Anal. Bioanal. Electrochem., Vol. 10, No. 4, 2018, 450-464

Analytical & Bioanalytical Electrochemistry

www.abechem.com

Full Paper

One-step Electrochemical Synthesis and Characterization of High Performance Magnetite/reduced Graphene Oxide Nanocomposite

Morteza Rezapour

IP Department, Research Institute of the Petroleum Industry (RIPI), P.O. Box 14665-137, Tehran, Iran

*Corresponding Author, Tel.: +98 21 48252228; Fax: +98 21 44739778

E-Mail: Rezapourm@ripi.ir

Received: 27 September 2017 / Received in revised form: 18 March 2018 / Accepted: 24 March 2018/ Published online: 30 April 2018

Abstract- Nanosized Fe_3O_4 particles were electrochemically prepared and deposited on reduced graphene oxide (rGO) sheets to prepare a nanocomposite for use in high performance capacitors. This was achieved using an electrophoretic/electrochemical deposition (EPD/ECD) approach for preparing the binder-free Fe_3O_4/rGO nanocomposite. The products were studies through XRD, IR, FE-SEM, VSM, TEM, and BET techniques. The mechanism of the formation of the nanocomposite through has also been described. The nancomposite further evaluated as an electrode material of use in supercapacitors and GCD tests indicated the composite to be able to deliver a specific capacitance (SC) of 478 F g^{-1} at 0.25 A g^{-1}. Electrodes based on the material was also found to have a cycle life of 87.4% after 5000 GCD cycles. The results indicated the positive effects as a result of the synergy between Fe_3O_4 and rGO.

Keywords- Iron oxide, Nanoparticles, Graphene oxide, Electrosynthesis, Nanocomposite, Supercapacitors

1. INTRODUCTION

Supercapacitors (SCs) are interesting tools due to their operability at high charge/discharge rates for very high cycles, as well as their ability to recover energy in

heavy-duty instruments and moderate costs [1]. The nature of the materials used in electrodes has a key role in the properties of supercapacitors and has direct influences on their energy storage abilities. Commonly three classes of materials, i.e. metal oxides/hydroxides, carbonous materials, and conductive polymers are used to construct supercapacitor electrodes. Transition metal oxides (TMOs) such as MnO_2 [2-4], Co_3O_4 [5-7], NiO [8-11], CuO [12] and Fe_3O_4 [13-17] have been proven to be promising material given their capability of reversible faradic charge storage, low costs, and their various valences. Specifically, Fe_3O_4 is considered a promising material for use as anode-material since it has a high theoretical energy capacity (2299 F/g), is cheap and abundant and does not have negative environmental impacts [18]. As in the case of other TMOs, Fe_3O_4 suffers low cycling stability and high-rate capability since it undergoes considerable expansion under charge/discharge operations and also has poor electrical conductivity [18-20]. In this light different approaches have been evaluated to overcome these shortcomings, which can be classified into preparation of nanostructures [21-23]; doping with metal ions [24-26]; and preparing Fe_3O_4/carbon hybrids [27-30].

On the other hand, cathodic electrochemical fabrication is a powerful method for preparing nanostructured materials for use in supercapacitors [30-35], which has not received the attention it deserves in areas like the preparation of composite materials [36-43], such as metal/metal oxides (hydroxides)/graphene-based hybrids. Electrophoretic deposition (EPD) is a further economical and versatile approach which can be used for depositing GO films of controlled thickness and morphology on various substrates [44,45], as well as the large-scale reinforcement of nanoparticles (NPs) in composites [45]. The method uses an electric field between electrodes, to drive NPs present in a suspension between anode/or cathode based on electrical charges.

The present work focuses on the combination of EPD and ECD to achieve a tool for the fabrication of electrode material. All studies in this area are have been based on the two-step fabrication of the metal oxide/graphene-based nanocomposites by an initial electrodesotion of the hydroxide/oxide on a graphene-based substrate [36,37], or electrostatic deposition procedures in a metal oxide/graphene dispersion [38,39], or the electrophoretic deposition of the carbon-based element followed by the electrochemical deposition of the desired metal oxide/hydroxide [40-43]. The present work uses a one-step electrophoretic/electrochemical co-deposition procedure which has not been used for preparing a Fe_3O_4/GO composite so far and hence this work can be considered as the first report on the co-deposition of a metal oxide/carbon hybrid through EP/EC.

2. EXPERIMENTAL PROCEDURE

2.1. Materials

$FeCl_2 \cdot 4H_2O$ (99.5%), $Fe(NO_3)_3 . 9H_2O$ (99.9%) were from Sigma Aldrich. Graphene oxide (GO) was obtained from the Research Institute of Petroleum Industry (IRIP). None of the materials was further treated before use.

2.2. Preparing Fe_3O_4 and Fe_3O_4/GO composite

Pristine Fe_3O_4 nanoparticles were prepared through a cathodic electrosynthesis (CE) approach reported in Refs. [46-49]. The typical two-electrode cell used to this end included a 2 cm^2 steel grid (cathode) located between two parallel graphite anodes and an NCF-PGS 2012 Potentiostat/Galvanostat electrochemical workstation system (Iran) was also used in its galvanostatic mode at 10 mA cm^{-2}. The deposition duration and temperature of the bath were 20 min and 25 ^oC. To prepare pristine Fe_3O_4, a solution of 0.4 g Fe(III) nitrate and 0.2 g Fe(II) chloride in 50 mL of deionized water was used, and Fe_3O_4/GO composite was prepared under similar conditions except for the fact that the solution contained 0.3 g GO before the dissolution of the two iron cations. The GO dispersion was preformed through probe sonication using Ultrasonic homogenizer, Development of Ultrasonic Technology Co., Iran. The mixture was then transferred to the electrodeposition bath and a current density of 10 mA cm^{-2} to the system. Once the deposition was over the grid was removed from the solution, repeatedly washed with deionized water and eventually dried at 70 ^oC for 1h. These assemblies (i.e. pristine Fe_3O_4@steel grid, and Fe_3O_4/GO@steel grid) were used as working electrodes (WEs) in the rest of capacitance experiments.

2.3. Characterization

Field-emission scanning electron microscopy (FE-SEM) analyses of the produced powders were performed on a Mira 3-XMU instrument under an accelerating voltage of 100 kV. X-ray diffraction analyses were also performed on a Phillips PW-1800 with a Co Kα radiation. Further, high resolution transmission electron microscopy (TEM) images were recorded on a Zeiss EM900 instrument at 80 kV. The hysteresis profiles of the samples were provided evaluated from −20000 to 20000 Oe under ambient conditions using a vibrational sample magnetometer (VSM, Meghnatis Daghigh Kavir Co. Iran). The specific surface area of the materials was determined using N2 adsorption–desorption isotherms at 77 K with the aid of a Quanta-chrome NOVA-2200e system and the FT-IR data were recorded in the range of 400-4000 cm^{-1}, on a Bruker Vector 22 spectrometer.

2.4. Electrochemical experiments

The electrochemical tests included cyclic voltammetry (CV) and galvanostatic charge/discharge (GCD) tests were performed using an AUTOLAB®, Eco Chemie, PGSTAT 30 and a three-electrode system (for the CV and GCD tests). The three electrode system was composed of a WE (i.e. the deposited nanocomposite onto steel grid), a reference electrode (i.e. Ag/AgCl reference) and a platinum wire as the counter electrode. The tests were performed in a 1 M aqueous solution of Na_2SO_3 as the electrolyte solution. The WEs had 2.5 and 2.2 mg of pristine Fe_3O_4 and Fe_3O_4/GO onto on the steel grids and the CVs were recorded from -1.0 to+0.1 V *vs*. Ag/AgCl at different the potential sweep values of 2, 5, 10, 20, 50 and 100 mV s^{-1}.

GCD experiments were performed under the current loads of 0.25, 0.5, 1, 2, 3 and 5 A g^{-1} in the potential window of -1.0 to 0V *vs*. Ag/AgCl. The EIS studies, on the other hand, were run in frequencies between 100 KHz and 0.01 Hz while applying 5 mV at the open-circuit potential. The SCs values were determined from the CV data using Eq. 1 [24]:

$$\mathrm{Cs(F\ g^{-1})} = \frac{\mathrm{Q}}{\mathrm{m\Delta\,(V)}},\ \ \mathrm{Q} = \int_{\mathrm{V_a}}^{\mathrm{V_a}} I(V)dV \qquad (1)$$

Where Cs illustrates the specific capacitance (F/g), *m* represents the electrode mass (g), v is the scan rate in the CVs (V/s), and (Va− Vc) is the potential window (V); and using the GCD data with Eq. 2 [35]:

$$Cs\ (F\ g^{-1}) = \frac{Q}{m\times\Delta V}\ , Q = I \times \Delta t \qquad (2)$$

Where Cs is the SC (F/g), I is the discharge current (A), m is the mass of the electrode (g), ΔV is the potential window (V), and Δt is the total discharge period (s).

3. RESULTS AND DISCUSSION

3.1. Structure and morphology

The X-ray diffraction patterns of pristine iron oxide and the composite (Fig. 1), both contain 9 peaks, which correspond to the (111), (220), (311), (400), (422), (511), (440), (620) and (533) planes of cubic Fe_3O_4 according to JCPDS no. 65-3107. This is proof of the magnetite crystal structure of both samples. Using the Debye–Scherrer equation (i.e. $D=0.9\lambda/\beta\cos(\theta)$; λ, β and θ expressing the X-ray wavelength, the full width of the diffraction line at half its maximum, and the diffraction angle) using the data of the diffraction line-width of (311) peak, the respective average crystallite sizes (D) of pristine Fe_3O_4 NPs and the Fe_3O_4 NPs were determined to be 7.2 nm and 9.3 nm.

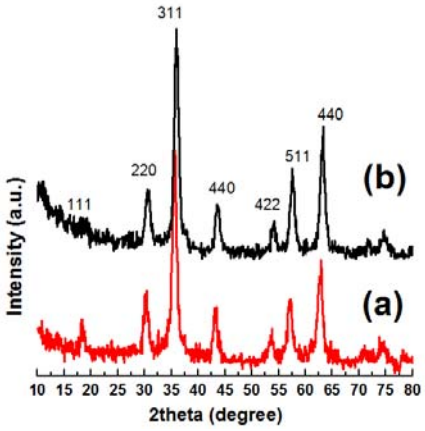

Fig. 1. XRD patterns of the electro-synthesized (a) pristine Fe_3O_4 and (b) Fe_3O_4/GO composite

The evolution of the chemical compositions of the the prepared samples were characterized by FT-IR, as can be seen in Fig. 2. The IR spectrum of pristine GO is also provided for the aim of comparison. The Ft-IR spectrum of pristine graphene oxide (Fig. 2a) reflcts the presence of a wide range of oxygen containing functional groups on the basal planes and edges of the, as well as peaks corresponding to the vibration modes of O-H, C=O, as well as carboxyl, epoxy and alcoxy C-O groups at 3405 cm^{-1}, at 1723 cm^{-1}, 1242 cm^{-1}, 1175 cm^{-1} and 1061 cm^{-1}, respectively [28,50,51].

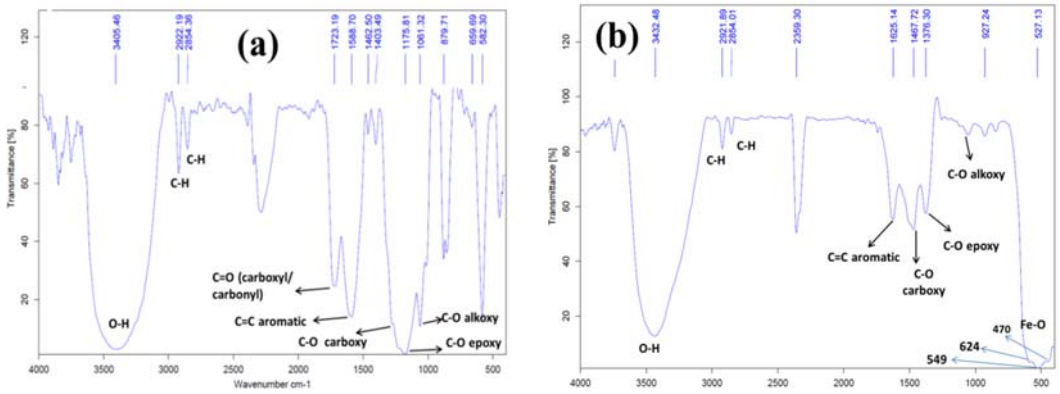

Fig. 2. IR spectra of (a) GO and (b) Fe_3O_4/rGO samples

Further, the strong stretching deformation of C=C of a honeycomb carbon network could be seen at 1628 cm^{-1}. In the case of the Fe_3O_4/rGO compositem all IR bands of GO and Fe_3O_4 could be seen (Fig. 2b). Yet the band corresponding to the carboxylic groups disapeared, which indicate that the that GO group is reduced. Furthermore, the FT-IR spectrum of the composite have three signals below 700 cm^{-1} (i.e. two strong bands at about

549 and 624 cm^{-1} corresponing to the splitting of the ν_1 band of the Fe—O bond; as well as a weaker bands at 470 cm^{-1} resulting from the ν_2 band of the Fe—O bond) [48,49]. Also two signals can be seen at around 1635 and 3447 cm^{-1}. These can be attributed to the stretching and deformation vibrations the surface bound –OH groups. The observations supported the presence of Fe_3O_4 phase in the fabricated composite. All in all these results were in favor of the formation of the Fe_3O_4/rGO composite. The FE-SEM of GO (Fig. 3a) clearly indicates the sample as having a sheet-like texture whit random aggregations and crumples.

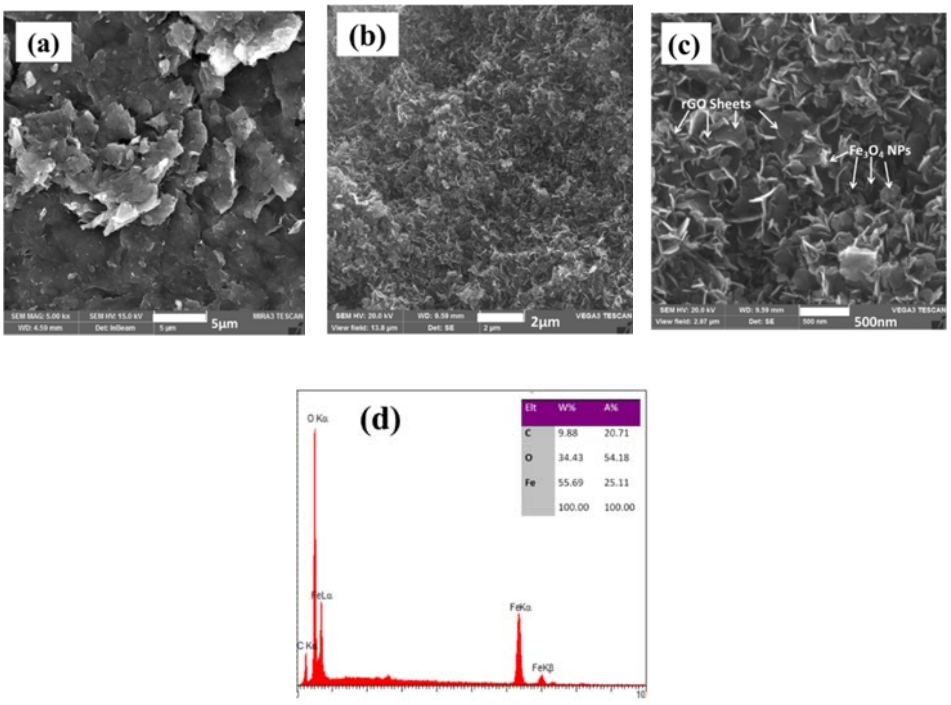

Fig. 3. FE-SEM images of (a) GO, and (b,c) Fe_3O_4/GO composite and (d) its EDS data

In the case of the composite (Figs. 3b and c) particle and sheet morphologies can be observed due to the presence of Fe_3O_4 and GO. The fully uniform texture of the sample Fig. 3b reflects the stable and regulated conditions of the electrophoretic deposition of GO on the steel grid (cathode) and the formation of the iron oxide NPs thereon.

Results obtained through energy-dispersive X-ray (EDX) (Fig. 3d) indicated the presence of Fe, O, and C at 55.69% wt., 9.88% wt., and 34.43% wt., respectively. Given that Fe_3O_4 contains 72.36% wt. of Fe and 27.64% wt. of O, the presence of C and the higher amount of O in the sample confirms the composition of Fe_3O_4/rGO. According to Fig. 3c, Fe_3O_4 NPs are present on the GO sheets, reflecting the formation and growth of the NPs on the electrophoretically deposited GO sheets present on the steel grid. Given these observations, the mechanism below was suggested for the formation of the composite (Fig. 4); GO can be easily dispersed in water by negatively charged carboxylic groups and has high electrical

mobility [40–42]. Therefore, in our used electrolyte i.e. aqueous solution of iron nitrate and iron chloride, and the GO sheets are well dispersed and their negatively charged carboxylic groups are bound to the ironically connected metal cations (Fe^{2+} and Fe^{3+}), as shown in (Fig. 4a). Once the electrodeposition starts, and voltage is applied between the electrodes, two processes are simultaneously started. These include (i) base (OH^-) electrogeneration due to the reduction of water molecules reduction on the cathode surface and (ii) the electrophoretic deposition of GO sheets as indicated in Fig. 4a. Notably, metal cations tend to move toward the cathode surface as the pH is increased, further creating an extra electrophoretic force on GO sheets in movement toward the steel grid (cathode). Hence, it is expected that GO sheet along with metal cations will move to the cathode surface. After each GO sheet is deposited on the cathode and with considering basic conditions, immediately two further simultaneous reactions processes are occurred on the cathode surface as noted in Fig. 4b. These are; (iii) chemical reactions of Fe^{2+} and Fe^{3+} with the hydroxide ions formed through electrogeneration, leading to the formation of the Fe_3O_4 deposit (i.e. $Fe^{2+} + 2Fe^{3+} + 8OH^- \rightarrow Fe_3O_4 + 4H_2O$), as well as the (iv) reduction of carboxylic groups present on the GO sheets and producing the reduced graphene oxide (rGO), as shown in Fig. 4b. In final, the composite of Fe_3O_4 nanoparticles grown on rGO sheets are formed on the cathode (Fig. 4b). This is completely supported by the TEM observations (Fig. 5). The TEM results show the presence of well dispersed rGO sheets containing NPs, 15nm in diameter (Fig. 5). The iron oxide NPs are well dispersed on the rGO sheet, preventing them from agglomerating due to their magnetic character. The lack of agglomeration allows the Fe_3O_4 NPs/rGO composite to have a high surface area (further confirmed by BET in Fig. 7), enhanced electrolyte penetration capability and supercapacitive behavior as opposed to Fe_3O_4 NPs. The high interface between rGO sheets and the Fe_3O_4 NPs enhances the conductivity of the NPs, which in turn provides higher storage properties in the case of the composite.

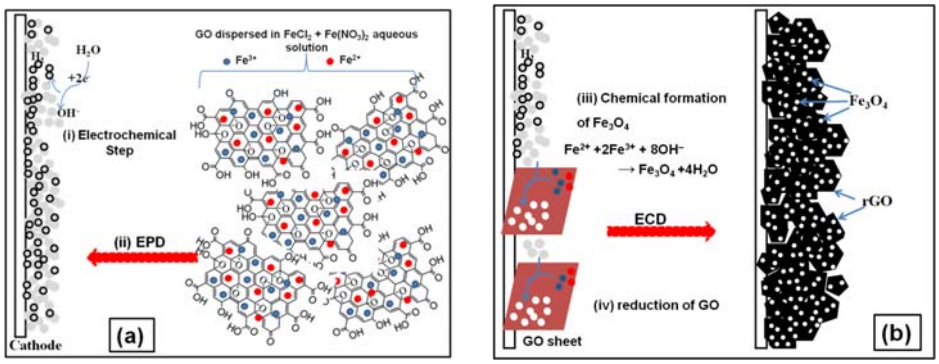

Fig. 4. (a,b) Schematic view of the EPD/ECD formation of Fe_3O_4/rGO composite

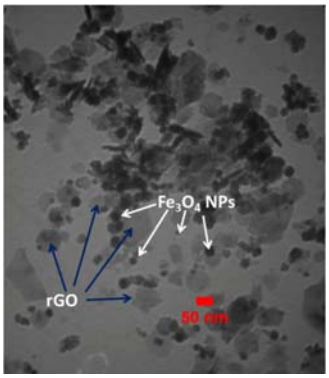

Fig. 5. TEM image of the prepared Fe_3O_4 NPs/rGO nanocomposite

The results of evaluating the magnetic properties of the samples through VSM measurements (Fig. 6) indicated *Ms*, *Mr* and H_{Ci} to be 72.1 emu g^{-1}, 0.72 emu g^{-1} and 18.55 G for the iron oxide particles, which are very close to the previously reported by this method [52-55], and 52.5 emu g^{-1}, 0.13 emu g^{-1} and 3.08 G for the composite, confirming the superparamagnetic qualities of both. The lower *Mr* and H_{Ci} of the composite, as opposed to pristine NPs indicate its better superparamagnetic nature.

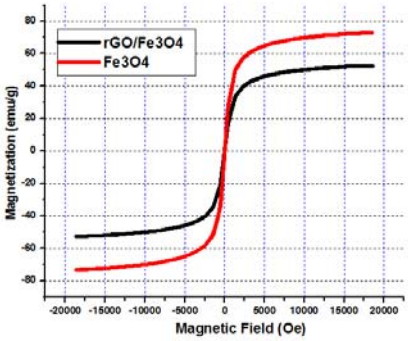

Fig. 6. Hysteresis loops for the prepared prsitine Fe_3O_4 NPs and (b) Fe_3O_4 NPs/rGO composite

Fig. 7 illustrates the N_2 isotherm and the pore size distribution profile of the composite. In the N_2 isotherm, a typical type II form and a type H3 hysteretic loop are observed which indicate the micro-porous nature of the sample. The mean pore diameter and the BET surface area of the composite (in Fig. 7) the respective values for these parameters were 6.19 nm and 255.71 m^2 g^{-1}, reflecting its higher surface area, as well as, larger pore diameter and volume. The enhanced surface area was attributed to the effect of the presence of GO during the electrosynthesis procedure.

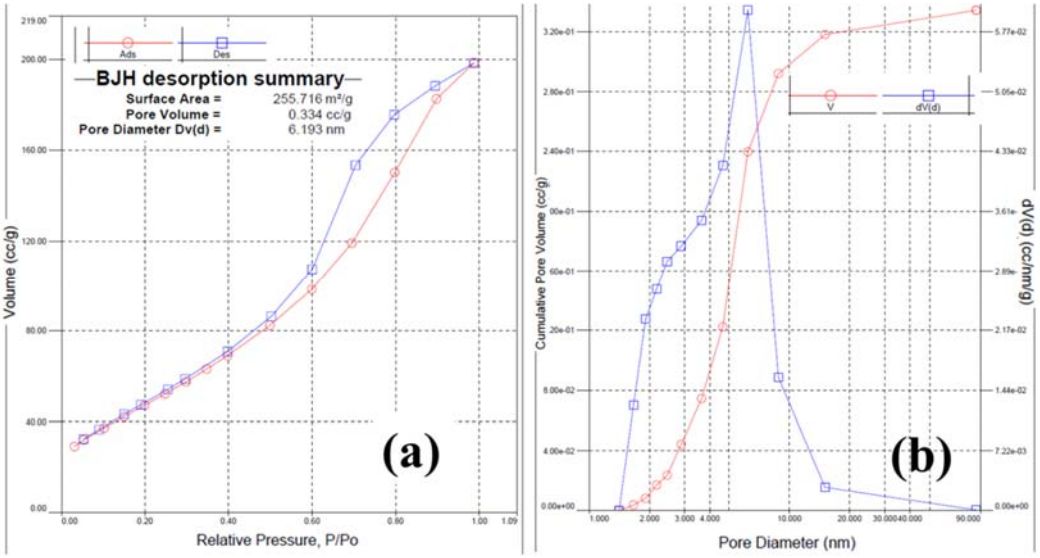

Fig. 7. BET and BJH pore size distribution curves of Fe_3O_4 NPs/ rGO composit

3.2. Capacitance studes

3.2.1. Cyclic voltammetry

The electrochemical behaviors of the WEs were evaluated through using them in a three-electrode system described above, using a 1 M Na_2SO_3 solution as the electrolyte. The CV curves obtained using the WEs loaded with pristine Fe_3O_4 and Fe_3O_4/rGO at 5 mV s, in the potential window of -1.0 to +0.2 V *vs.* Ag/AgCl can be seen in Fig. 8a. Both curves have a typical pseudocapacitance shape, a good faradic peaks and the electric double layer behavior. According to the literature, in the case of Fe_3O_4 as the active material in Na_2SO_3 electrolyte a combination of double layer and Faradic charge storage mechanisms exist [17-19]. The former capacitance mechanism is due to the reduction/oxidation of the SO_3^{2-} anions adsorbed onto the Fe_3O_4 [18]:

$$2SO_3^{2-} + 3H_2O + 4e^- \leftrightarrow S_2O_3^{2-} + 6OH^- \quad (3)$$

$$S_2O_3^{2-} + 3H_2O + 8e^- \leftrightarrow 2S^- + 6OH^- \quad (4)$$

According to Fig. 8a, both WEs revealed the charge storage behavior of Fe_3O_4, which is a shared ingredient. In the case of the composite coated WE the current-potential response was stronger and the CV curve is wider which is attributed to the presence of rGO, which acts as a conductive substrate for Fe_3O_4 NPs, and also contributes in the charge storage performance through an independent EDL mechanism. Hence the composite WE provide higher SCs. The shape of the CVs of the Fe_3O_4/rGO WE recorded at various scan rates of 2-100 mV s^{-1} (Fig. 8b) clearly reveals a pseudocapacitive behavior at the higher scan rates.

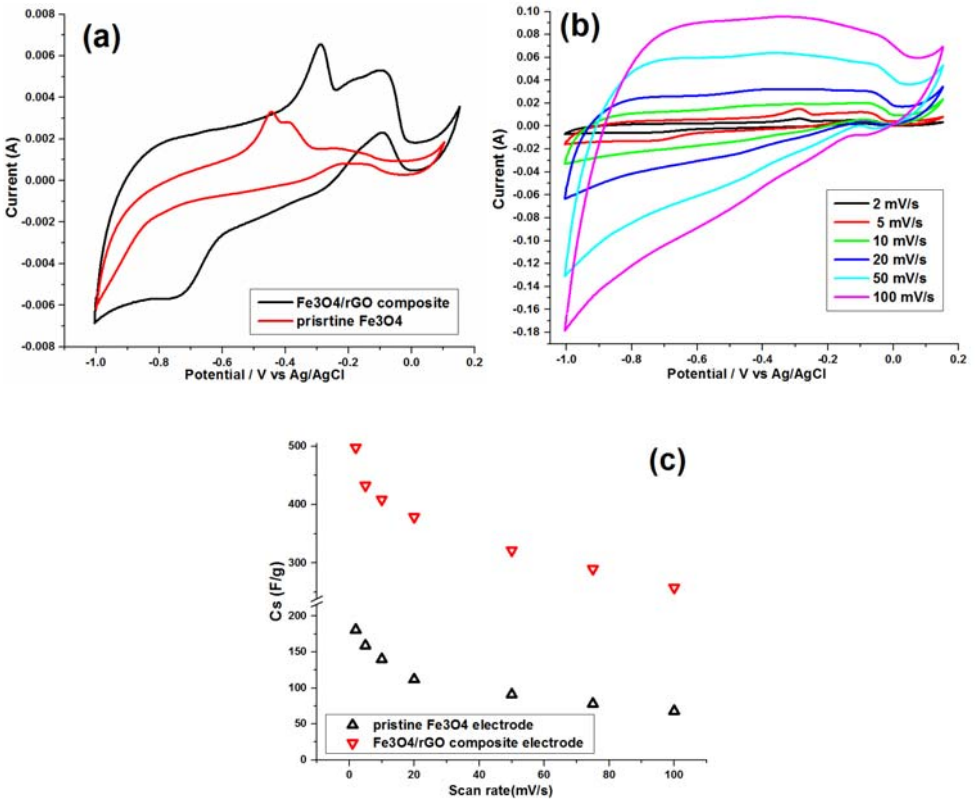

Fig. 8. CVs of of (a) pristine Fe_3O_4 NPs and (c,d) Fe_3O_4 NPs/rGO composit, (c) the calculated Cs values *vs*. scan rate for both electrodes

The *SC* values of the composite WE were calculated from the CVs using Eq. (1) and were plotted against the scan rate (Fig. 8c). SC data for the pristine Fe_3O_4 WEs were also obtained from a previous reprot for the purpose of comparison [17,52]. Based on the calciulations the Fe_3O_4/rGO electrode could deliver respective *SC* values of 497.1, 432.7, 408.2, 379.2, 322.6, 290.4 and 258.3 F g^{-1} at 2, 5, 10, 20, 50, 75 and 100 mV s^{-1}. While these values were 175, 152, 143, 109, 90, 85 and 71 F g^{-1} at of 2, 5, 10, 20, 50 and 100 mV s^{-1} for a pristine iron oxide WE, which are very close to the data reported in literature [52-55], indicating that the Fe_3O_4/rGO composite WE has high performance. In other words, the supercapacitive performance of Fe_3O_4 is enhanced in the presence of rGO, which is attributed to the well dispersion of the oxide NPs onto rGO sheets and the high interfacial area between the sheets and the NPs (as shown by TEM results, Fig. 5), as well as the high surface area and large pore size of the composite as indicated by BET results (Fig. 7).

3.2.2. Charge-discharge experiments

Galvanostatic charge-discharge (GCD) experiments were carried out in a current load window of 0.25 to 10 A g^{-1} on both the composite and pristine Fe_3O_4 WEs and the results are

given in Fig. 9. Fig. 9a shows that the Fe_3O_4/rGO electrode has a better charge-discharge ability as reflected by its longer charge and discharge times, in comparison to the pristine Fe_3O_4 WE, and it is hence expected to exhibit better charge storage ability and CS values.

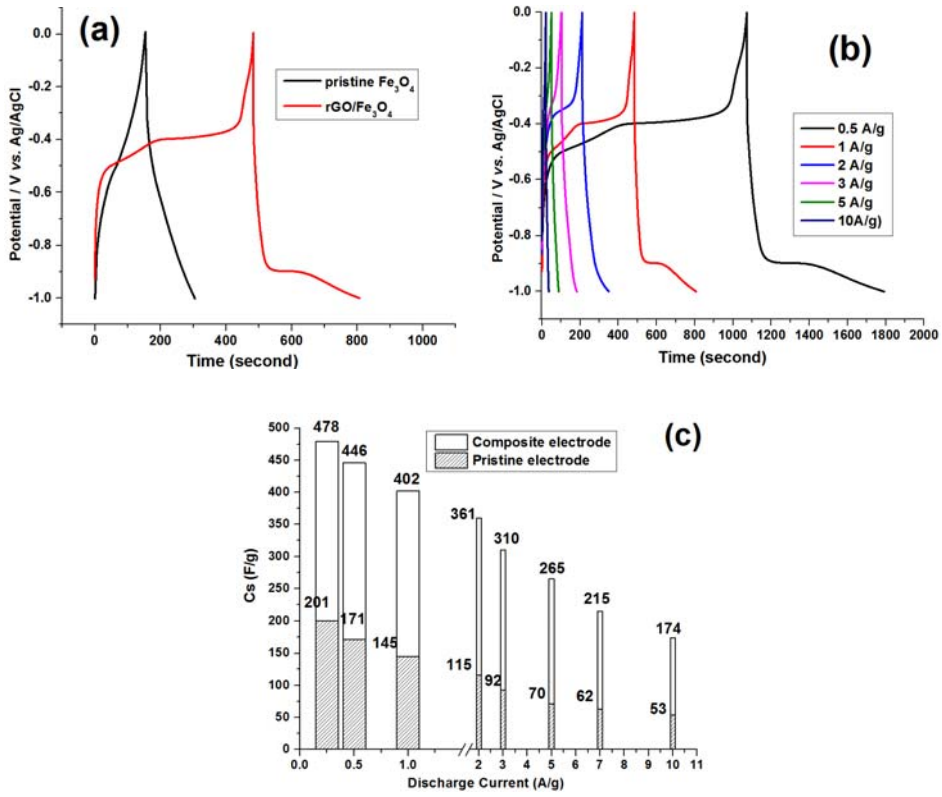

Fig. 9. (a) GCD profiles for pristine Fe_3O_4 and Fe_3O_4/rGO electrodes at the current load of 1 A/g and (b) the GCD profiles of Fe_3O_4/rGO at various current loads and (c) calulated specific capacity values for both electrodes at the different charge-discharge rates

Fig. 9b illustrates the GCD profiles of the Fe_3O_4/rGO WE at various charge-discharging rates, indicating that the shape of GCD curve remains, which can be attributed to the good capacitive performance of the composite material even at high discharging rates. The *SC* values obtained for the Fe_3O_4/rGO WE were determined through Eq. (2), and these data are presented in Fig. 9c, together with the data on pristine Fe_3O_4 WE obtained from our previous works [17,52]. In the case of pristine iron oxide WE, SC values of 201 F g^{-1}, 171 F g^{-1}, 145 F g^{-1}, 115 F g^{-1}, 92 F g^{-1}, 70 F g^{-1}, 62 F g^{-1} and 53 F g^{-1} has been reported at discharging loads of 0.25, 0.5, 1, 2, 3, 5, 7 and 10 A g^{-1}, respectively [52,55]. Based on calculations, the Fe_3O_4/rGO composite was found to be able to deliver capacitance of 478 F g^{-1}, 446 F g^{-1}, 402 F g^{-1}, 361 F g^{-1}, 310 F g^{-1}, 265 F g^{-1}, 215 F g^{-1} and 174 F g^{-1} at the respective discharging loads of 0.25, 0.5, 1, 2, 3, 5, 7 and 10 A g^{-1}. The values are very close to those obtained from CVs (Fig. 8c), reflecting the good supercapacitive behavior of the

nanocomposite. The SCs obtained for the composite WEs were much greater than those of the pure Fe_3O_4 WE (Fig. 9c). The findings reveal the positive synergy between Fe_3O_4 and rGO, which arises from the uniform anchoring of the Fe_3O_4 NPs on rGO sheets and suppressing of the re-stacking of rGO due to the presence of the Fe_3O_4 NPs, availability of the highly conductive electronic network for the redox process of Fe_3O_4 particles by rGO sheets, and avoiding the volume change and agglomeration of the NPS due to the presence of rGO. All of these enhance the interface area of the rGO and the NPs, providing more accessible ionic/electronic transport mechanisms and improving the poor electrical and charge transfer properties of Fe_3O_4. Additionally the charge storage ability of the composite was comparable with those of other rGO/Fe_3O_4 electrodes in Table 1.

Table 1. Electrochemical capacitance values reported for Fe_3O_4/rGO composites

Fe_3O_4 structure type	**Electrolyte**	**Current density (A/g)**	**Specific capacitance (F/g)**	**Ref.**
N-doped G- Fe_3O_4/ CNTs	1 M Na_2SO_4	0.5	418	[14]
3D Fe_3O_4/rGO	2 M KOH	3.6	455	[27]
RGO/Fe_3O_4/PANI	0.5 M H_3PO_4	1	283	[28]
Fe_3O_4/rGO	1 M KOH	1	241	[50]
Fe_3O_4/rGO	6 M KOH	3A	782	[51]
Fe_3O_4@rGO	6 M KOH	1	216.7	[53]
Fe_3O_4/rGO	6 M KOH	0.2	350.6	[54]
pure Fe_3O_4	1 M Na_2SO_3	1	145	[55]
Fe_3O_4/rGO	1 M Na_2SO_3	1	402	This work

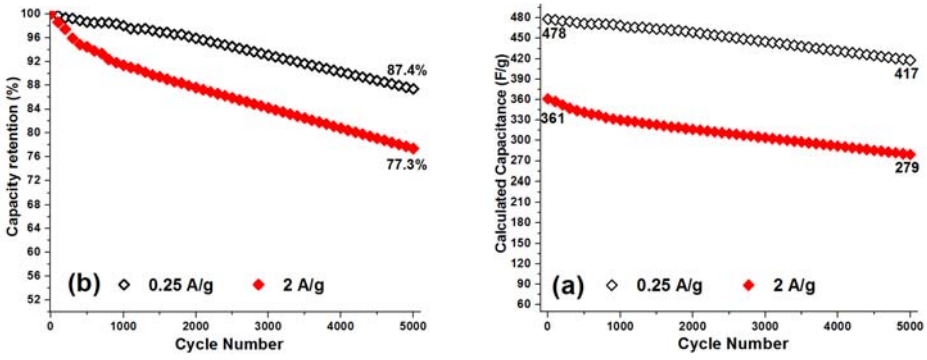

Fig. 10. Calculated capaciatnces and the capacity loss for the fabricated composite during 5000 continus GCD cycling at the discharge loads of 0.25 and 2 A g^{-1}

The composite WE was subjected to 5000 cycles at current loads of 0.25 and 2 A g^{-1} in a 1 M Na_2SO_3 electrolyte and the SC and capacity retentions at each cycle were calculated and plotted in Fig. 10. The data revealed that the capacitance values reduced from 478 F g^{-1} to 417 F at 0.25 A g^{-1} and form 361 F g^{-1} to 279 F g^{-1} at current load of 2 A g^{-1}, during the 5000 cycles, which is equivalent to cycling abilities of 87.4% and 77.3%. Pristine Fe_3O_4 WEs were formerly reported a being able to deliver cycling performances of 77.6% and 60.4% under identical conditions [52,55]. Comparing the data confirms the improved cycling ability in the case of the composite.

4. CONCLUSION

A novel and facile co-deposition strategy (i.e. EPD/ECD) was used for depositing a Fe_3O_4/rGO composite onto a steel substrate. FE-SEM and TEM tests confirmed the simultaneous deposition of rGO sheets and the electrochemical formation of iron oxide NPs on these sheets. Given the results of the observations, a detailed mechanism was proposed for the formation of the composite. CV and GCD evaluations proved the high supercapacitive ability of the composite, and hence the one-pot EPD/ECD procedure was concluded as a facile synthesis route for preparing binder-free iron oxide/carbonous hydride electrodes for various applications.

REFERENCES

[1] A. González, E. Goikolea, J. Andoni Barrena, and R. Mysyk, Renew. Sust. Energy Rev. 58 (2016) 1189.

[2] G. A. M. Ali, M. M. Yusoff, E. R. Shaaban, and K. F. Chong, Ceram. Int. 43 (2017) 8440.

[3] M. Aghazadeh, A. Bahrami-Samani, D. Gharailou, M. G. Maragheh, and M. R. Ganjali, J. Mater. Sci.: Mater. Electron. 27 (2016) 11192.

[4] M. Aghazadeh, M. R. Ganjali, and P. Norouzi, J. Mater. Sci.: Mater. Electron.27 (2016) 7707.

[5] A. García-Gómez, S. Eugénio, R. G. Duarte, T. M. Silva, and M. F. Montemor, Appl. Surf. Sci. 382 (2016) 34.

[6] M. Aghazadeh, R. Ahmadi, D. Gharailou, M. R. Ganjali, and P. Norouzi, J. Mater. Sci.: Mater. Electron. 27 (2016) 8623.

[7] M. Gopalakrishnan, G. Srikesh, A. Mohan, and V. Arivazhagan, Appl. Surf. Sci. 403 (2017) 578.

[8] G. Srikesh, and A. Samson Nesaraj, Ceram. Int. 42 (2016) 5001.

[9] A. Barani, M. Aghazadeh, M. R. Ganjali, B. Sabour, A. A. M. Barmi, and S. Dalvand, Mater. Sci. Semiconductor Processing 23 (2014) 85.

[10] M. Aghazadeh, J. Mater. Sci.: Mater. Electron. 28 (2016) 3108.
[11] H. Xiao, F. Qu, and X. Wu, Appl. Surf. Sci. 360 (2016) 8.
[12] Y. Zhang, W. W. Guo, T. X. Zheng, Y. X. Zhang, and X. Fan, Appl. Surf. Sci. 427 (2018) 1158.
[13] M. Aghazadeh, I. Karimzadeh, and M. R. Ganjali, J. Mater. Sci.: Mater. Electron. 28 (2017) 13532.
[14] A. Babu Ganganboina, A. D. Chowdhury, and R. Doong, Electrochim. Acta 245 (2017) 912.
[15] M. Aghazadeh, J. Mater. Sci.: Mater. Electron. 28 (2017) 18755.
[16] X. Zeng, B. Yang, X. Li, R. Li, and R. Yu, Mater. Design 101 (2016) 35.
[17] M. Aghazadeh, and M. R. Ganjali, J. Mater. Sci. 53 (2018) 295.
[18] V. D. Nithya, and N. S. Arul, J. Mater. Chem. A 4 (2016) 10767.
[19] M. Melake Mezgebe, Z. Yan, G. Wei, S. Gong, and H. Xu, Mater. Today Energy 5 (2017) 164.
[20] Y. Z. Wu, M. Chen, X. H. Yan, J. Ren, and X. N. Cheng, Mater. Lett. 198 (2017) 114.
[21] J. Ma, J. Chang, H. Ma, D. Zhang, and S. Wang, J. Colloid Interface Sci. 498 (2017) 282.
[22] R. Zhao, X. Shen, Q. Wu, X. Zhang, W. Li, G. Gao, L. Zhu, L. Ni, G. Diao, and M. Chen, ACS Appl. Mater. Interfaces 9 (2017) 24662.
[23] X. Yu, M. Wang, A. Gagnoud, Y. Fautrelle, R. Moreau, and X. Lia, Electrochim. Acta 248 (2017) 150.
[24] M. Aghazadeh, and M. R. Ganjali, J. Mater. Sci.: Mater. Electron. 29 (2018) 2291.
[25] M. Aghazadeh, I. Karimzadeh, and M. R. Ganjali, J. Mater. Sci.: Mater. Electron. 28 (2018) 19061.
[26] M. Aghazadeh, and I. Karimzadeh, Mater. Res. Express 4 (2017) 105505.
[27] R. Kumar, R. K. Singh, A. R. Vaz, R. Savu, and S. A. Moshkalev, ACS Appl. Mater. Interfaces 9 (2017) 8880.
[28] S. Mondal, U. Rana, and S. Malik, J. Phys. Chem. C 121 (2017) 7573.
[29] L. Wang, Jie Yu, X. Dong, X. Li, Y. Xie, S. Chen, P. Li, H. Hou, and Y. Song, ACS Sust. Chem. Eng. 4 (2016) 1531.
[30] A. Kumar Das, S. Sahoo, P. Arunachalam, S. Zhang, and J. J. Shim, RSC Adv. 6 (2016) 107057.
[31] J. Talat Mehrabad, M. Aghazadeh, M. Ghannadi Maragheh, and M. R. Ganjali, Mater. Lett. 184 (2016) 223.
[32] M. Aghazadeh, A. A. M. Barmi, H. M. Shiri, and S. Sedaghat, Ceram. Int. 39 (2013) 1045.
[33] M. Aghazadeh, M. R. Ganjali, and P. Noruzi, Thin Solid Films 634 (2017) 24.
[34] M. Aghazadeh, and M. R. Ganjali, J. Mater. Sci.: Mater. Electron. 28 (2017) 8144.

[35] M. Aghazadeh, J. Mater. Sci.: Mater. Electron. 28 (2017) 3108.
[36] C. Liu, K. Wang, S. Luo, Y. Tang, and L. Chen, Small 7 (2011) 1203.
[37] B. Yuan, C. Xu, D. Deng, Y. Xing, L. Liu, H. Pang, and D. Zhang, Electrochim. Acta 88 (2013) 708.
[38] S. Hassan, M. Suzuki, and A. Abd El-Moneim, Int. J. Electrochem. Sci. 9 (2014) 8340.
[39] M. Li, X. Bo, Z. Mu, Y. Zhang, and L. Guo, Sensors and Actuators B 192 (2014) 261.
[40] Rusi, and S.R. Majid, Scientific Reports 5 (2015)16195.
[41] S. Ghasemi, R. Hosseinzadeh, and M. Jafari, Int. J. Hydrogen Energy 40 (2015) 1037.
[42] Y. Zhao, D. Zhao, P. Tang, Y. Wang, C. Xu, and H. Li, Mater. Lett. 76 (2012) 127.
[43] P. Asen, S. Shahrokhian, and A. Irajizad, Int. J. Hydrogen Energy 42 (2017) 21073.
[44] A. Chavez-Valdez, M. S. P. Shaffer, and A. R. Boccaccini, J. Phys. Chem. B 117 (2013) 1502.
[45] M. Diba, D. W. H. Fam, A. R. Boccaccini, and M. S. P. Shaffer, Prog. Mater. Sci. 82 (2016) 83.
[46] M. Aghazadeh, Mater. Lett. 211 (2018) 225.
[47] M. Aghazadeh, I. Karimzadeh, M. R. Ganjali, and M. G. Maragheh, J. Mater. Sci.: Mater. Electron. 29 (2018) 5163.
[48] M. Aghazadeh, and I. Karimzadeh, Curr. Nanosci. 14 (2018) 42.
[49] M. Aghazadeh, I. Karimzadeh, M. Ganjali, D. Gharailou, and P. Kolivand, Curr. Nanosci.13 (2017) 274.
[50] L. Li, P. Gao, S. Gai, F. He, Yujin Chen, M. Zhang, and P. Yang, Electrochim. Acta 190 (2016) 566.
[51] S. Saha, M. Jana, P. Samanta, N. C. Murmu, N. H. Kim, T. Kuila, and J. H. Lee, RSC Adv. 4 (2014) 44777.
[52] M. Aghazadeh, and M. R. Ganjali, Ceram. Int. 44 (2018) 520.
[53] T. Liu, X. Zhang, B. Li, J. Ding, Y. Liu, G. Li, X. Meng, Q. Cai, and J. Zhang, RSC Adv. 4 (2014) 50765.
[54] T. Qi, J. Jiang, H. Chen, H. Wan, L. Miao, and L. Zhang, Electrochim. Acta 114 (2013) 674.
[55] M. Aghazadeh, I. Karimzadeh, and M. R. Ganjali, J. Electron. Mater. 47 (2018) 3026.